Fermi Surface and Positron Annihilation in Yttrium*

T. L. Loucks
Institute for Atomic Research and Department of Physics, Iowa State University, Ames, Iowa
(Received 1 November 1965)

The electronic structure of yttrium has been calculated at the equivalent of 6000 general points in the primitive Brillouin zone using the augmented-plane-wave method. The density of states and the Fermi surface are presented. The topology of the Fermi surface is discussed, and experimental results for de Haas–van Alphen measurements are predicted. Wave functions have also been calculated for each of the occupied eigenvalues, and these were used to study the angular distribution of radiation resulting from positron annihilation in the metal. Few experimental results are currently available for comparison with this work.

I. INTRODUCTION

THIS is a theoretical study of the electronic structure of yttrium. It is based on augmented-plane-wave (APW) calculations using the original method proposed by Slater.[1] The electronic structure of yttrium is interesting because of the *s-d* character of the energy bands. The atomic configuration of yttrium is $4d5s^2$, and it has a hexagonal close-packed crystal structure. It is very similar to the heavier $4f$ rare earth metals which have atomic configuration $5d6s^2$ and the same crystal structure. Yttrium, however, is not complicated by either magnetic or relativistic effects, and by studying it we gain valuable information to assist in the interpretation of results for the rare earths.

The report begins in the next section with some preliminary remarks on procedure. The ingredients of the APW calculation are briefly discussed. Following this the results are presented in two parts: the Fermi surface and the Fermi sea. The second of these includes results which depend on the eigenvalues and wave functions beneath the Fermi energy, such as density of states and angular distribution of positron annihilation radiation. In the final section these results are discussed; this discussion is necessarily brief because of the unavailability of related experimental results.

II. PROCEDURE

The electronic structure was determined by an APW calculation using 22 reciprocal lattice vectors in the wave-function expansion. The 22 reciprocal lattice vectors were chosen by a convergence study at symmetry points. They represent the minimum set required for accurate results throughout the 1/24 zone for energies below the Fermi energy. They are listed in Table I. The lower half of the primitive Brillouin zone is shown in Fig. 1. The reciprocal-lattice basis vectors are

$$\begin{aligned}\mathbf{K}_1&=(2\pi/c)\hat{e}_3\,,\\ \mathbf{K}_2&=(2\pi/a\sqrt{3})(\sqrt{3}\hat{e}_1+\hat{e}_2)\,,\\ \mathbf{K}_3&=(4\pi/a\sqrt{3})\hat{e}_2\,,\end{aligned}\qquad(1)$$

where $\hat{e}_1$, $\hat{e}_2$, and $\hat{e}_3$ are unit vectors in the x, y, and z directions, respectively. The lattice constants a and c are listed in Table II.

The 1/24 zone is outlined by points of high symmetry and is shown in Fig. 2. For this calculation the 1/24 zone was divided into 10 layers. Each of these layers was partitioned into 25 triangular microzones. All of the states in each of these microzones were represented by a typical centrally located point. This established a grid of 250 distinct points in the 1/24 zone. The eigenvalues below the Fermi energy were determined to 5-place accuracy at each of the 250 grid points using the 22 APW expansion. The expansion coefficients were also determined for each eigenvalue by inverting the secular equations. The muffin-tin potential used in these calculations was constructed in the usual manner from a superposition of atomic potentials[2] including exchange in the $\rho^{1/3}$ approximation. The APW sphere radius is

TABLE I. Reciprocal lattice vectors used in APW expansion.

$(ijk)=i\mathbf{K}_1+j\mathbf{K}_2+k\mathbf{K}_3$						
$(\bar{2}00)$	$(\bar{2}\bar{1}1)$	$(\bar{2}\bar{1}0)$				
$(\bar{1}00)$	$(\bar{1}\bar{1}1)$	$(\bar{1}\bar{1}0)$	$(\bar{1}0\bar{1})$	$(\bar{1}1\bar{1})$	$(\bar{1}10)$	$(\bar{1}01)$
(000)	$(0\bar{1}1)$	$(0\bar{1}0)$	$(00\bar{1})$	$(01\bar{1})$	(010)	(001)
(100)	$(1\bar{1}1)$	$(1\bar{1}0)$	$(10\bar{1}$			
(200)						

TABLE II. Some parameters used in the APW calculation, in atomic units.

Lattice constants	$a=6.871$ (a.u.)
	$c=10.89$
APW sphere radius	$R=2.858$

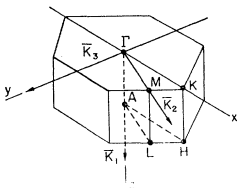

FIG. 1. Lower half of primative Brillouin zone for the hexagonal close-packed crystal structure with the 1/24 zone outlined by points of high symmetry.

* Work was performed at the Ames Laboratory of the U. S. Atomic Energy Commission, Contribution No. 1813.
[1] J. C. Slater, Phys. Rev. **51**, 846 (1937).
[2] D. Liberman, J. T. Waber, and Don T. Cromer, Phys. Rev. **137**, A27 (1965).

given in Table II. The results obtained from the eigenvalues and wave functions are presented in the following section.

III. RESULTS

1. Fermi Surface

The Fermi energy was determined by arranging in increasing order the eigenvalues from the 250 points in in the 1/24 zone. Because there are 3 valence electrons/atom and 2 atoms/unit cell, the lowest 750 eigenvalues are occupied (each one accepting two electrons of opposite spin). The highest occupied energy was 0.474 Ry. The energy of the lowest state at Γ was 0.137 Ry which yields a bandwidth of 0.337 Ry.

Intersections of the Fermi surface with the faces of the 1/24 zone are shown in Fig. 3. Intersections with the 10 planes indicated on Fig. 2 are shown in Fig. 4. The Fermi surface consists of two pieces: an electron surface centered along the ΓA axis and a hole surface at the edge of the primitive zone centered along the KH axis. If spin-orbit interaction is neglected, the two pieces of Fermi surface are in contact along the base of the zone outlined by symmetry points AHL. For this reason it is convenient to display the Fermi surface using the double-zone representation. By referring to an orbit on the electron (hole) surface we shall mean that the orbit encloses an electron (hole) region in the double-zone representation.

A model of the hole region in this representation is shown in Fig. 5. In the extended double-zone scheme the hole region resembles an underground cavern. The various levels of the cavern are connected by small vertical shafts in the floors and ceilings along the KH axes. Alternate levels of the cavern have nearly flat floors and ceilings joined by thick cylindrical columns along the ΓA axes. On the other levels the columns are much bigger and the walls are fluted; the ceilings and floors are marked by occasional depressions. It will be convenient in the discussion of orbits on the Fermi surface to designate these two different levels in some manner. Let us designate as level A the upper level in Fig. 5. The lower level with the fluted walls and irregular floor and ceiling will be designated as level B. A cast of the floor (or ceiling) of level B is shown in Fig. 6. It is easier to visualize some orbits on the Fermi surface by considering this portion of the electron surface. The vertical shafts connecting A levels with B levels along the KH axes are only partially shown in Fig. 6 at the corners and in the center of the figure.

In the following paragraphs some of the extremal cross sections of the Fermi surface and some possible orbits will be discussed. The cross-sectional areas are related to de Haas–van Alphen frequencies in the inverse magnetic field by

$$f = 374.1 \times 10^6 \times \text{extremal area}, \qquad (2)$$

where the area is in a.u.$^{-2}$ and the frequency is in gauss.

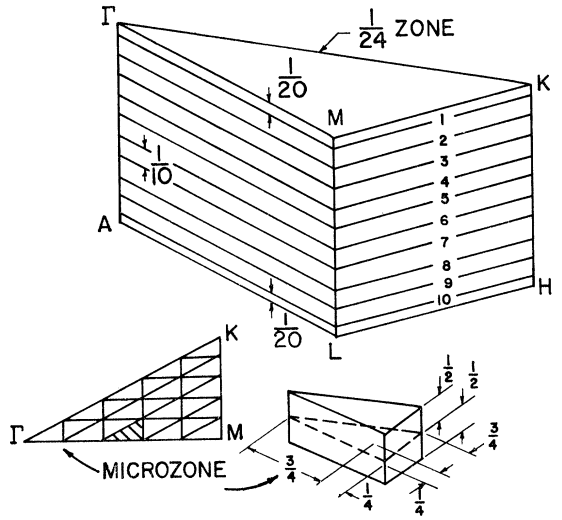

FIG. 2. 1/24th zone showing calculation mesh for general points.

It will be convenient to refer to de Haas–van Alphen frequencies instead of the corresponding extremal area.

There are four extremal areas perpendicular to the (0001) direction (along ΓA). There are two extremals on the cylindrical columns in level A: one (call it α) around the midsection and the other (call it β) corresponding to layer 4 in Fig. 2. There is a third extremal (call it γ) around the midsection of the fluted column in level B. These three orbits are on the hole surface. The fourth extremal perpendicular to the (0001) direction (call it δ) is on the thin vertical shafts of the electron surface. These shafts extend between the two levels A and B. The de Haas–van Alphen frequencies corresponding to these extremal areas are given in Table III. The shape of the orbits is shown in Fig. 7.

Perpendicular to the $(10\bar{1}0)$ direction (along ΓM) there is an extremal orbit which runs along the floor of

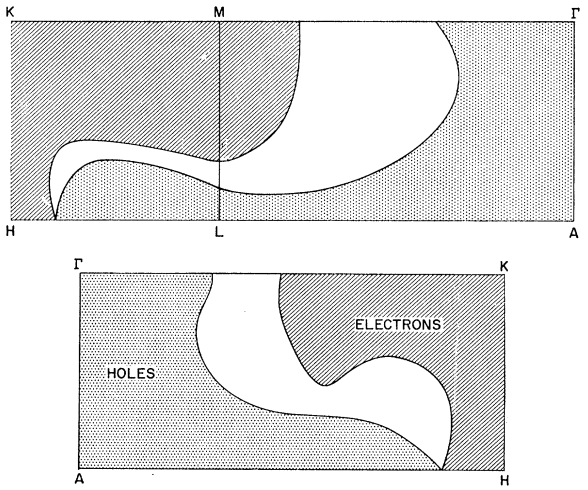

FIG. 3. Intersections of the Fermi surface with faces of the 1/24 zone.

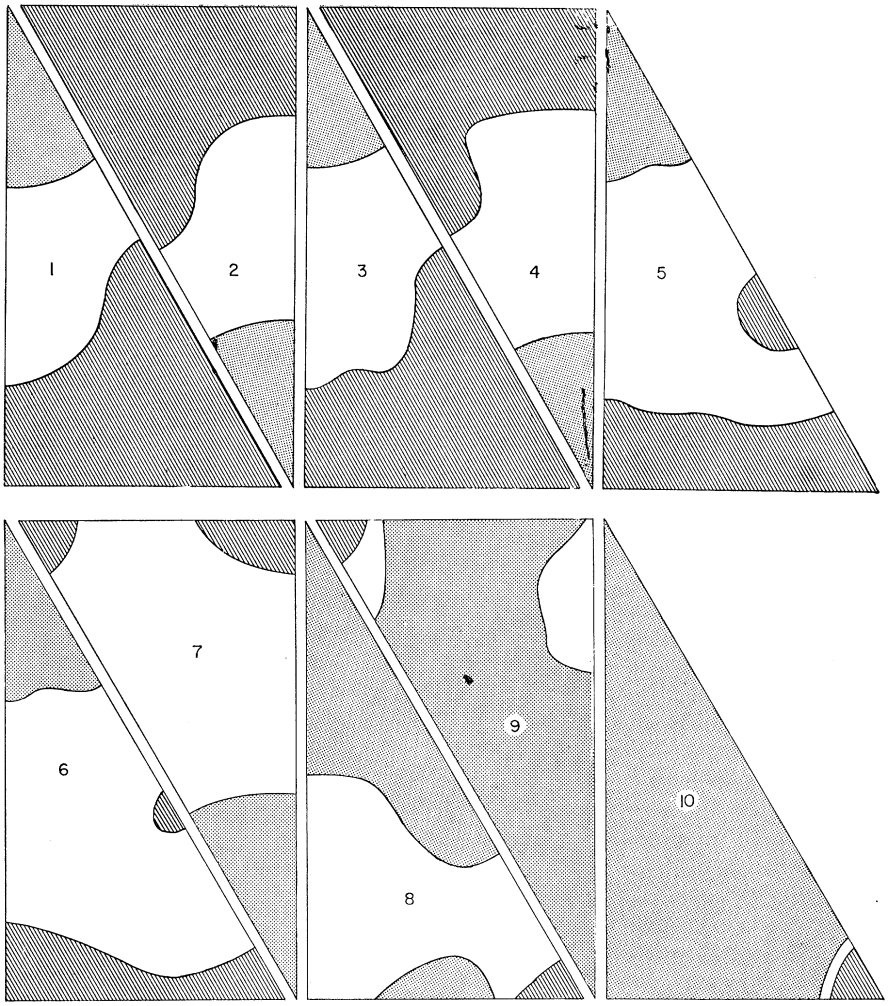

FIG. 4. Intersections of the Fermi surface with the planes shown in Fig. 2.

level A from a point along the ML axis toward the vertical shafts along the KH axes. The orbit passes down these two adjacent vertical shafts and across the ceiling of level B. This hole orbit is designated by ϵ. With fields sufficiently large for magnetic breakdown the most probable orbit would have a frequency of 33×10^6 G. For low fields the spin-orbit splitting on the basal plane AHL would restrict the orbits to a particular zone and two different frequencies would be possible: 26×10^6 G for the first zone orbit and 39×10^6 G for the second zone orbit.

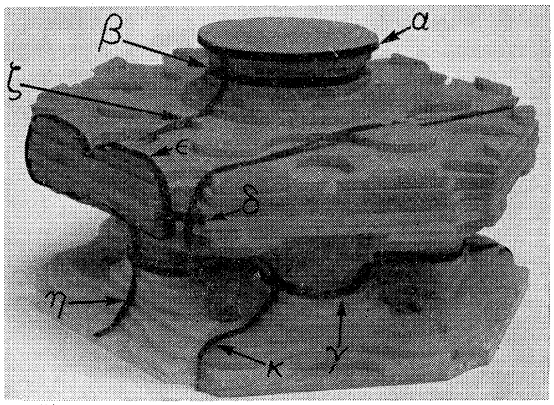

FIG. 5. Model of the hole region in the double-zone representation.

TABLE III. de Haas–van Alphen frequencies predicted from the Fermi surface of yttrium.

Magnetic field direction	Orbits Designation	Orbits Type	Frequency (10^6 G)
(0001)	α	hole	46
	β	hole	35
	γ	hole	149
	δ	electron	3.1
$(10\bar{1}0)$	ϵ	hole	33[a]
$(11\bar{2}0)$	ζ	electron	115
	η	electron	30
	θ	electron	56
	κ	hole	204
19° from $(11\bar{2}0)$ to $(10\bar{1}0)$	λ	electron	75

[a] 26 and 39 also possible.

There are also open orbits in planes perpendicular to the $(10\bar{1}0)$ direction. One of these runs along the $(11\bar{2}0)$ direction (along IK) across the floor of level A connecting points on the ML symmetry axes without passing through the KH axes. The other open orbit perpendicular to the $(10\bar{1}0)$ direction runs along the (0001) direction. In the high-field limit this orbit extends down the cylindrical column in level A (along the intersection of the Fermi surface with the ΓKHA plane) and into level B along the vertical shafts centered along the KH axes. The orbit continues along the fluted columns in level B and through the vertical shafts into level A again. Without magnetic breakdown the orbit would still be open but restricted to passing only through level A or level B.

There are several closed orbits perpendicular to the $(11\bar{2}0)$ direction (along ΓK). There is an electron orbit which passes along the floor and ceiling of level A between neighboring cylindrical columns. This orbit (call it ζ) follows the intersection of the Fermi surface with the ΓMLA plane. A similar electron orbit (call it η) exists on level B. This orbit is easily pictured around the middle of the "arms" of the electron surface shown in Fig. 6. The corresponding de Haas–van Alphen frequencies are given in Table III.

There is another extremal orbit on the "arms" of the electron surface. This orbit is designated as θ and passes over four peaks as indicated in Fig. 6. Also there is an extremal hole orbit which passes along the floor of level A, down two vertical shafts which are symmetrically located with respect to the ΓH axis, down the walls of the fluted column in level B, through the vertical shafts in the floor and across the ceiling of level A. This orbit is designated by κ. As can be seen in Fig. 7, it is a large orbit. It is possible, however, that this orbit will not be experimentally observed. There are not many neighboring orbits with approximately the same area because of the limitation that the orbits pass through the small shafts linking the two levels.

There is one additional extremal orbit which should be mentioned. Consider an axis approximately 19° from the $(11\bar{2}0)$ direction toward the $(10\bar{1}0)$ direction. There is a plane perpendicular to this and passing through the symmetry point M which cuts across four peaks of the electron surface. This orbit is designated as λ and is shown in Fig. 6. The expected de Haas–van Alphen frequency for this and the other extremal orbits are given in Table III.

There are two open orbits in a plane perpendicular to the $(11\bar{2}0)$ direction. They both extend along the $(10\bar{1}0)$ direction and pass through adjacent ML axes One of these passes along the floor (and ceiling) of level A and the other similarly in level B.

2. Fermi Sea

The density-of-states curve is shown in Fig. 8. We see that for the lower energies the density of states is

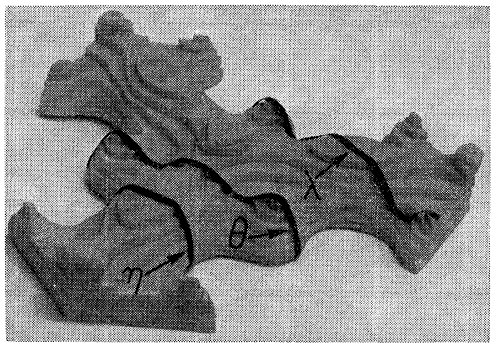

FIG. 6. Model of a portion of the electron region in the double-zone representation.

generally less than the free-electron value. At the higher energies the more narrow d bands contribute a large number of states, greatly increasing the density of states above the free-electron values. At the Fermi energy the density of states is 26.8 electrons/atom Ry. This yields an electronic specific-heat coefficient of $\gamma=11.2\times10^{-4}$ cal/mole deg^2. In the same units the free-electron value is 3.46×10^{-4} and the experimental result is 24.4×10^{-4}.[3] The factor of 3.2 between the APW and free-electron results is due to the d-band contribution. The factor of about 2 between the experimental and APW results is presumably due to the electron-phonon interaction. An APW calculation by Dimmock and Freeman[4] for gadolinium gave $\gamma=10\times10^{-4}$ cal/mole deg^2. This was also found to be 3 times larger than the free-electron value and smaller than experiment by about a factor of 2. This points out the strong similarity between the electronic structures of yttrium and the heavier $4f$ rare earths. A further similarity can be seen in the density-of-states curve for gadolinum given by these same authors.[4]

The electronic structure can also be observed in the angular distribution of positron-annihilation radiation from the crystal. This has been calculated using the 22

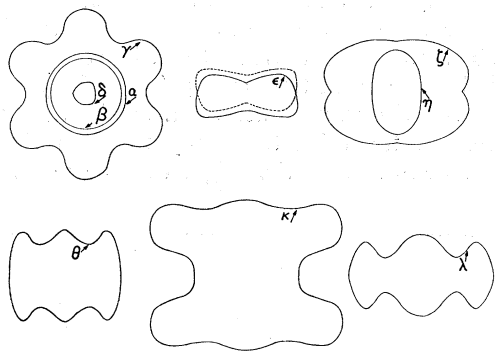

FIG. 7. Shapes of extremal orbits on the Fermi surface.

[3] H. Montgomery and G. P. Pells, Proc. Phys. Soc. (London) 78, 622 (1961).
[4] J. O. Dimmock and A. J. Freeman, Phys. Rev. Letters 13, 750 (1964).

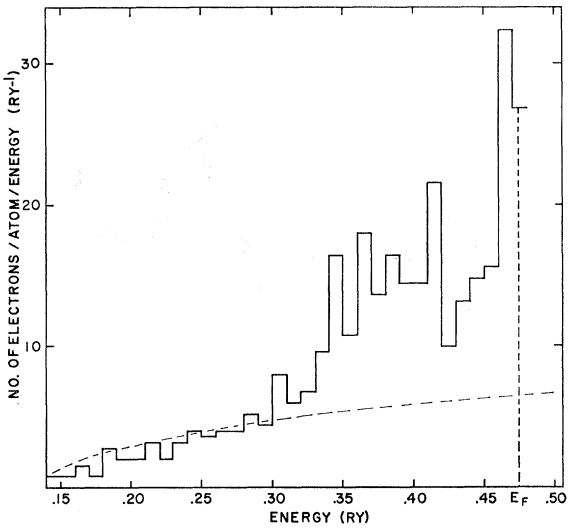

FIG. 8. Density-of-states curve for yttrium. Solid line is APW result, and broken line is from free-electron model.

APW expansions for the electron wave functions and the Wigner-Seitz model for the positron wave function. The theoretical aspects of the method are discussed in the Appendix. The final result is given in Eq. (A16). In the free-electron (free-positron) model only the first term in this equation would be present. The other two terms can be thought of as subtracting from the free-electron result the contributions from inside the APW spheres and replacing them with the more realistic orbital nature of the electronic wave function in the ion-core region. These terms also take into account the repulsion of the positron from the screened nuclear charge. This effect can be seen in Fig. 9 where the numerical solution for the positron wave function is shown.

The overlap between the electron, positron, and photon wave functions in the ion-core region is given by Eq. (A15). Typical results of this l-dependent function (they also depend on the characteristic energy) are shown in Fig. 10. It can be seen that the contributions from large momenta and large arguments are relatively small. This enables us to truncate the inner summation over $\mathbf{K}$ in the second term of Eq. (A16). Only the 19 reciprocal-lattice vectors nearest a particular $\mathbf{g}$ were included. In the third term only the 19 reciprocal lattice vectors nearest the origin were included. The resulting angular distribution of annihilation radiation is given in Fig. 11.

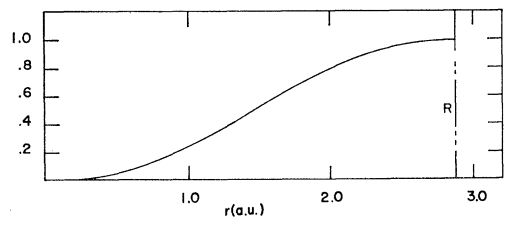

FIG. 9. Numerical solution of positron wave function in yttrium. Eigenvalue is 0.791 Ry.

IV. DISCUSSION OF RESULTS

There are no experimental results available which relate directly to the Fermi surface of yttrium. Correlation with experiment is possible only for the angular distribution from annihilation radiation. The experimental results of Williams and Mackintosh[5] are shown in Fig. 11. There is agreement on the two main features: the photon yield for small momenta drops sharply below the free-electron parabola, and this is followed by a hump due to the d-band contributions. The experimental results are for holmium, but we have already seen the strong similarity between yttrium and the heavier $4f$ rare-earth metals. This similarity is even more evident in our preliminary unpublished results on the Fermi surface and density of states in holmium.[5a] The similarity between these experimental results and the theoretical calculation is very gratifying for two reasons. It shows that electron-positron correlation (which was neglected in the calculation) apparently removes from the experimental results very little of the information about the electronic structure. The agreement also lends support to the other theoretical results and indicates that at least the general features of the Fermi surface should be correct.

It is, however, possible that some of the more subtle features of the Fermi surface will have to be modified when experimental data become available. The most sensitive region is at the edge of the zone near the symmentry points H and L. The energy bands in this region are very flat, and small changes in the potential would be strongly reflected in the shape of the Fermi surface. It is possible, for instance, that the vertical shafts along the KH axes are not present. This would result in the

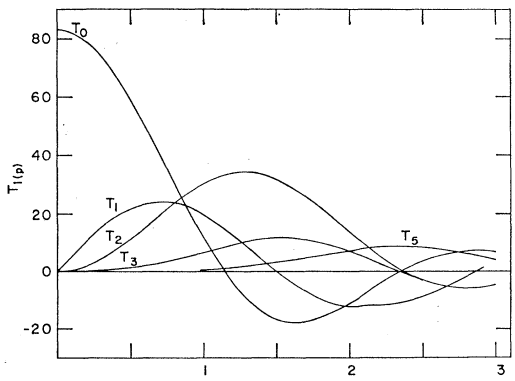

FIG. 10. Typical results for the function $T_l(p)$ defined by Eq. (A15).

[5] R. W. Williams, T. L. Loucks, and A. R. Mackintosh, Phys. Rev. Letters **16**, 168 (1966).

[5a] *Footnote added in proof.* Reference 5 contains more recent theoretical results on holmium and experimental results for yttrium.

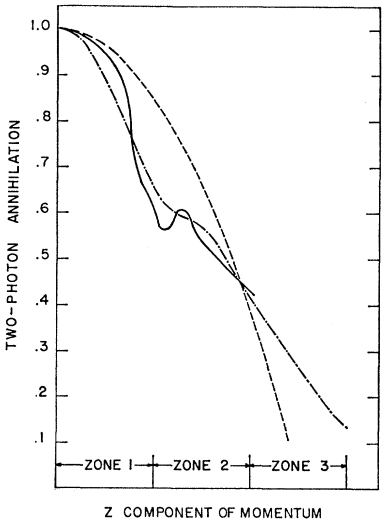

FIG. 11. Angular distribution of radiation from two-photon positron annihilation. Solid line is present result for yttrium (*c*-axis orientation); dashed curve is free-electron (free-positron) parabola; dot-dashed curve is experimental results for holmium (Ref. 5) (*c*-axis orientation).

absence of the low-frequency de Haas–van Alphen signal from the δ orbit (See Fig. 5). Absence of these shafts would also eliminate the ϵ and κ orbits as well as the open orbit perpendicular to the $(10\bar{1}0)$ direction which runs along the (0001) direction.

APPENDIX

The probability that an electron with wave vector $\mathbf{k}$ will annihilate with a thermalized positron and yield a photon pair with center-of-mass momentum $\mathbf{p}$ is proportional to[6]

$$F(\mathbf{p},\mathbf{k})=\left|\int\psi(\mathbf{k},\mathbf{r})\psi_+(\mathbf{r})e^{-i\mathbf{p}\cdot\mathbf{r}}d^3r\right|^2, \qquad \text{(A1)}$$

where the integration is over the entire crystal. Here $\psi(\mathbf{k},\mathbf{r})$ and $\psi_+(\mathbf{r})$ are the electron and positron wave functions, respectively. In the usual rectangular slit apparatus all photon pairs with a particular component of center-of-mass momentum are measured, and the yield is proportional to

$$N(p_z)=\int\int_{-\infty}^{\infty}dp_x dp_y\sum_{\mathbf{k}}F(\mathbf{p},\mathbf{k}), \qquad \text{(A2)}$$

where the summation is over all occupied states.

In order that our method will be applicable to metals with energy bands of *s-d* character, the electronic wave functions are approximated by a linear combination of APW's. We write this as

$$\psi(\mathbf{k},\mathbf{r})=\sum_{\mathbf{g}}\mathfrak{A}(\mathbf{g},\mathbf{k})\mathrm{APW}(\mathbf{k}+\mathbf{g}), \qquad \text{(A3)}$$

where

$$\mathrm{APW}(\mathbf{k})=e^{i\mathbf{k}\cdot\mathbf{r}}, \qquad \text{(A4)}$$

[6] S. De Benedetti, C. E. Cowan, W. R. Konneker, and H. Primakoff, Phys. Rev. **77**, 205 (1950).

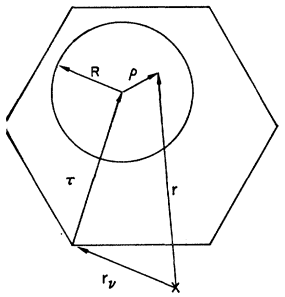

FIG. 12. Hypothetical unit cell showing coordinate system used in the Appendix.

outside the spheres, and

$$\mathrm{APW}(\mathbf{k})=4\pi e^{i\mathbf{k}\cdot(\mathbf{r}_\nu+\boldsymbol{\tau})}\sum_{lm}i^l j_l(kR)\times\frac{U_l(\rho)}{U_l(R)}Y_{lm}^*(\hat{k})Y_{lm}(\hat{\rho}) \qquad \text{(A5)}$$

inside the sphere at $\mathbf{r}_\nu+\boldsymbol{\tau}$. Solutions of the radial Schrödinger equation (regular at the origin) in the spherically symmetric electronic potential are denoted $U_l(\rho)$. The dependence on the characteristic energy is suppressed for convenience. In Fig. 12 we show $\mathbf{r}_\nu$ as the lattice vector to the νth unit cell. $\boldsymbol{\tau}$ is a vector pointing to the center of the APW sphere of radius R. The radial coordinate centered on the APW sphere is denoted by $\boldsymbol{\rho}$. The expansion coefficients in Eq. (A3) are determined in the usual manner from the variational principle. The secular determinant is solved for the eigenvalues, and for each of these the expansion coefficients are determined by inverting a set of simultaneous nonhomogeneous equations.

Since the APW's are based on the muffin-tin potential, it is natural to approximate the positron wave function in a similar potential. In the present calculation a muffin-tin potential was constructed for the positron

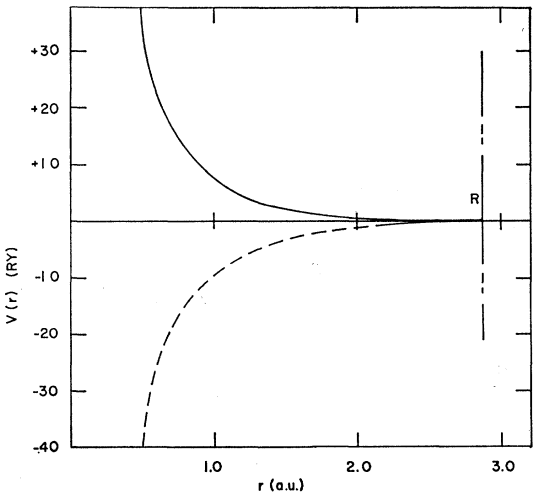

FIG. 13. Muffin-tin potentials. Broken line is electronic potential (with exchange) and solid line is positronic potential (without exchange).

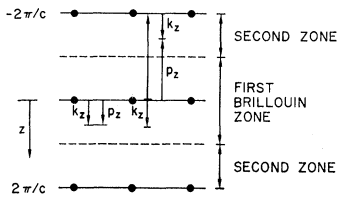

FIG. 14. Cross section of hexagonal close-packed reciprocal lattice with z direction taken along the c axis.

using the same APW sphere as for the electrons. The exchange contribution was not included in the positron potential. The two muffin-tin potentials are shown in Fig. 13. In the region of constant potential (adjusted to zero) the positron wave function is taken to be unity. Inside the APW spheres it is the ground-state solution to the radial Schrödinger equation (regular at the origin) which satisfies the following boundary conditions:

$$\psi_+(R)=1 \quad \text{and} \quad \psi'_+(R)=0. \tag{A6}$$

The numerical solution for the positron wave function is shown in Fig. 9.

Next let us consider the volume integral in Eq. (A1). Both the electron wave function and the positron wave function have different forms inside and outside the APW spheres. It is therefore convenient to express the integral over the crystal as the sum of two contributions, one from inside (V_i) and one from outside (V_0) the spheres. The contribution from outside the spheres is found by extending the form of the wave functions in this region throughout the entire crystal [call this V_0 (crystal)] and subtracting the resulting contributions from the regions inside the spheres [call this V_0 (spheres)]. Equation (A1) can then be written

$$F(\mathbf{p},\mathbf{k})=|V(\mathbf{p},\mathbf{k})|^2, \tag{A7}$$

where

$$V(\mathbf{p},\mathbf{k})=V_i+V_0(\text{crystal})-V_0(\text{spheres}). \tag{A8}$$

Using $\psi_+(\rho)=1$ for $\rho\geqslant R$ and Eq. (A4) for the electron wave function, it is easy to show that

$$V_0(\text{crystal})=N\Omega_0\sum_{\mathbf{g}}\mathfrak{A}(\mathbf{g},\mathbf{k})\delta(\mathbf{k}+\mathbf{g}-\mathbf{p}), \tag{A9}$$

where N is the number of units cells in the crystal and Ω_0 is the unit-cell volume. Using the same form of the wave functions inside the spheres we find

$$V_0(\text{spheres})=\sum_{\text{spheres}}^{\text{crystal}}\int\sum_{\mathbf{g}}\mathfrak{A}(\mathbf{g},\mathbf{k})e^{i(\mathbf{k}+\mathbf{g}-\mathbf{p})\cdot\mathbf{r}}d^3r, \tag{A10}$$

where the integration is over a typical sphere. By changing variables (See Fig. 12) this integration can be centered on the spheres, and we find

$$V_0(\text{spheres})=N\sum_{\mathbf{g}}\sum_{\mathbf{K}}\mathfrak{A}(\mathbf{g},\mathbf{k}) \times\delta(\mathbf{k}+\mathbf{g}-\mathbf{p}-\mathbf{K})S(\mathbf{K})\frac{4\pi R^2 j_1(KR)}{K}, \tag{A11}$$

where the structure factor is given by

$$S(\mathbf{K})=\sum_{\text{spheres}}^{\text{cell}}e^{i\mathbf{K}\cdot\tau}. \tag{A12}$$

Using $\psi_+(\rho)$ to designate the numerically tabulated positron wave function inside the spheres and taking Eq. (A5) for the electron wave function, the contribution to the volume integral from inside the spheres is given by

$$V_i=\sum_{\text{spheres}}^{\text{crystal}}\int\sum_{\mathbf{g}}\mathfrak{A}(\mathbf{g},\mathbf{k})\psi_+(\rho)4\pi e^{i(\mathbf{k}+\mathbf{g})\cdot(\mathbf{r}_\nu+\tau)} \times\sum_{lm}i^l j_l(|\mathbf{k}+\mathbf{g}|R)\frac{U_l(\rho)}{U_l(R)} \times Y_{lm}^*(\hat{k}_g)Y_{lm}(\hat{\rho})e^{-i\mathbf{p}\cdot\mathbf{r}}d^3r, \tag{A13}$$

where $\hat{k}_g$ is the unit vector along $\mathbf{k}+\mathbf{g}$. Expanding the plane wave in spherical harmonics and using the orthogonality relations between these functions, this becomes

$$V_i=N\sum_{\mathbf{g}}\sum_{\mathbf{K}}\mathfrak{A}(\mathbf{g},\mathbf{k})\delta(\mathbf{k}+\mathbf{g}-\mathbf{p}-\mathbf{K})S(\mathbf{K}) \times\sum_l(2l+1)j_l(|\mathbf{k}+\mathbf{g}|R)T_l(p)P_l(\hat{k}_g\cdot\hat{p}). \tag{A14}$$

For convenience the function $T_l(p)$ has been defined by

$$T_l(p)=4\pi\int r^2\psi_+(r)j_l(pr)\frac{U_l(r)}{U_l(R)}dr. \tag{A15}$$

Equation (A8) can now be written (N has been dropped)

$$\begin{aligned}V(p,k)=&\Omega_0\sum_{\mathbf{g}}\mathfrak{A}(\mathbf{g},\mathbf{k})\delta(\mathbf{k}+\mathbf{g}-\mathbf{p})\\&+\sum_{\mathbf{g}}\mathfrak{A}(\mathbf{g},\mathbf{k})\sum_{\mathbf{K}}\delta(\mathbf{k}+\mathbf{g}-\mathbf{p}-\mathbf{K})S(\mathbf{K})\\&\times\sum_l(2l+1)j_l(|\mathbf{k}+\mathbf{g}|R)T_l(p)P_l(\hat{k}_g\cdot\hat{p})\\&-\sum_{\mathbf{g}}\mathfrak{A}(\mathbf{g},\mathbf{k})\sum_{\mathbf{K}}\delta(\mathbf{k}+\mathbf{g}-\mathbf{p}-\mathbf{K})S(\mathbf{K})\\&\times\frac{4\pi R^2 j_1(KR)}{K}.\end{aligned} \tag{A16}$$

The delta functions appearing in Eq. (A16) can be used to eliminate the two integrations and the z component of the $\mathbf{k}$ summation indicated in Eq. (A2) providing that certain restrictions are placed on the reciprocal lattice expansions $\sum(\mathbf{g})$ and $\sum(\mathbf{K})$. As an example let us consider the hexagonal close-packed crystal structure. The reciprocal lattice consists of evenly spaced planes of hexagonal grids perpendicular to the c axis. In Fig. 14 we show a cross section of this reciprocal lattice with the z direction taken along the c axis. For p_z in the first zone ($0\leqslant p_z\leqslant\pi/c$) we can take $k_z=p_z$. The first term in Eq. (A16) then contributes to $N(p_z)$ in Eq. (A2) only if $g_z=0$. The integrals over p_x and p_y eliminate the corresponding components of the

delta function. The second and third terms in Eq. (A16) can also be simplified. They will contribute to $N(p_z)$ only if $g_z=K_z$ and $p_i=k_i+g_i-K_i$ for $i=x$ and y. Thus, for each term in the summation $\sum(\mathbf{g})$ it is only necessary to sum those reciprocal lattice vectors which have the same z component. Similar remarks hold for p_z in the higher zones. By choosing k_z and p_z so that they differ by appropriate reciprocal lattice vectors, it is only necessary to consider k_z in the first Brillouin zone. For instance, with p_z in the second zone, it is possible to take $p_z=k_z-2\pi/c$ (See Fig. 14). The first term in Eq. (A16) contributes to $N(p_z)$ in this case only if $g_z=-2\pi/c$. The second and third terms contribute only if $K_z=g_z+2\pi/c$ (the same relationships for p_x and p_y given above still holding).

ACKNOWLEDGMENTS

It is a pleasure to thank Dr. A. R. Mackintosh and R. W. Williams for making their very interesting positron-annihilation results available prior to publication. I would also like to thank J. J. Hinrichsen and R. E. Bergin, Jr., for technical assistance.

PHYSICAL REVIEW VOLUME 144, NUMBER 2 15 APRIL 1966

Computer Simulation of Vacancy Migration*

J. H. WEINER AND W. F. ADLER†
Columbia University, New York, New York
(Received 12 November 1965)

An idealized model for a vacancy in a crystal lattice which permits vacancy migration is presented. It consists of a linear chain of atoms together with a substrate potential, with piecewise linear force laws between nearest-neighbor atoms and between atoms and substrate. The predictions of the Vineyard equilibrium rate theory are calculated explicitly for this model. A computer simultation procedure is described which reproduces some, although not all, of the statistical characteristics of thermal equilibrium. The jump rates observed in the simulation agree reasonably well with those predicted by the Vineyard theory.

1. INTRODUCTION

THE process of thermally activated defect motion in crystals presents a many-body problem of considerable complexity. Its analysis requires (1) idealization in the formulation of the mathematical model, in particular regarding the nature of the interatomic forces and (2) simplifying assumptions regarding the statistical aspects of the process. In a direct comparison of a given theoretical prediction with experiment it is frequently difficult to separate discrepancies due to the idealizations of the first class and those due to the assumptions of the second.

In the present work we have undertaken the computer simulation of the behavior of an idealized crystal model. Since the interatomic force laws of the model are precisely defined, there is no uncertainty in the observed behavior to be attributed to this account, and attention may be focused on the statistical aspects of the problem.

Among the extensive theoretical treatments of defect motion in crystals two distinct approaches, characterized in the literature generally by the terms equilibrium and dynamical theories, may be distinguished. For a description and comparison of these two types of theories, the reader is referred to the literature[1] on the subject. We have chosen here to make a comparison of the prediction of the equilibrium theory for an idealized model, from the many-body viewpoint presented by Vineyard,[2] with the computer simulation results for the same model. The most serious question which has been raised regarding the Vineyard equilibrium theory refers to the statistical aspects of the process during the period in which the system has left the potential well and is surpassing the saddle point.[3] Accordingly, in the computer simulation, the statistical criteria to be satisfied were prescribed only for the period in which the system was in the neighborhood of the well; the statistical aspects of the motion when the system left the well were then determined by the dynamics of the model and could be observed. Also observed were the jump rates, and these were compared with those predicted for the model by the Vineyard theory.

The plan of this paper is as follows: The crystal model employed is described in Sec. 2. It consists of a linear chain of atoms containing a vacancy together

* This research was supported by the U. S. Air Force Office of Scientific Research under Grant No. AF-AFOSR-228-63.

† Present address: Battelle Memorial Institute, Columbus, Ohio.

[1] D. Lazurus, in *Advances in Solid State Physics*, edited by F. Seitz and D. Turnbull (Academic Press Inc., New York, 1960), Vol. 10, p. 71; P. G. Shewmon, *Diffusion in Solids* (McGraw-Hill Book Company, Inc., New York, 1963).

[2] G. H. Vineyard, J. Phys. Chem. Solids **3**, 121 (1957).

[3] S. A. Rice, Phys. Rev. **112**, 804 (1958). The author states his view as follows: "A major point of departure between Vineyard's treatment and that presented herein is that Vineyard's treatment is in the sense of transition state theory and still makes use of the assumption that the state at the top of the col is sufficiently long-lived to permit the definition of thermodynamic functions. The author cannot prove or disprove this assumption, but his personal prejudice is that it is not accurate for the case of diffusion."

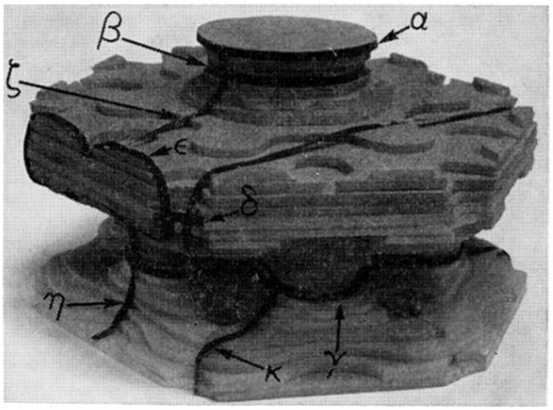

FIG. 5. Model of the hole region in the double-zone representation.

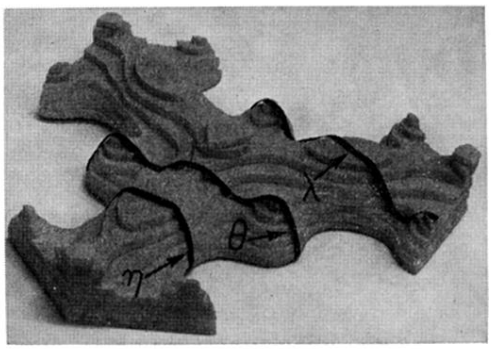

FIG. 6. Model of a portion of the electron region in the double-zone representation.